Integration of a deep-learning-based fire model into a global land surface model

Authors: Rackhun Son[1,*], Tobias Stacke[2], Veronika Gayler[2], Julia E.M.S. Nabel[1,2], Reiner Schnur[2], Lazaro Alonso Silva[1], Christian Requena-Mesa[1], Alexander J. Winkler[1], Stijn Hantson[3], Sönke Zaehle[1], Ulrich Weber[1] and Nuno Carvalhais[1,4,5]

[1]Max Planck Institute for Biogeochemistry, Jena, Germany.

[2]Max Planck Institute for Meteorology, Hamburg, Germany.

[3]Faculty of Natural Sciences, Universidad del Rosario, Bogotá, Colombia.

[4]ELLIS Unit Jena, Jena, Germany.

[5]Departamento de Ciências e Engenharia do Ambiente, Faculdade de Ciências e Tecnologia, Universidade Nova de Lisboa, Caparica, Portugal.

*Correspondence to: Rackhun Son (rackhun@bgc-jena.mpg.de)

Key Points:

- Deep neural networks (DNN) can accurately predict global burnt area fraction on a daily scale.
- Integration of the DNN in a physics-based land model significantly improves fire-driven loss in vegetation dynamics.
- The DNN accounts for regional fire variations by assigning varying degrees of importance to each predictor.

Abstract

Fire is a crucial factor in terrestrial ecosystems playing a role in disturbance for vegetation dynamics. Process-based fire models quantify fire disturbance effects in stand-alone dynamic global vegetation models (DGVMs) and their advances have incorporated both descriptions of natural processes and anthropogenic drivers. Nevertheless, these models show limited skill in modeling fire events at the global scale, due to stochastic characteristics of fire occurrence and behavior as well as the limits in empirical parameterizations in process-based models. As an alternative, machine learning has shown the capability of providing robust diagnostics of fire regimes. Here, we develop a deep-learning-based fire model (DL-fire) to estimate daily burnt area fraction at the global scale and couple it within JSBACH4, the land surface model used in the ICON ESM. The stand-alone DL-fire model forced with meteorological, terrestrial and socio-economic variables is able to simulate global total burnt area, showing 0.8 of monthly correlation (r_m) with GFED4 during the evaluation period (2011-15). The performance remains similar with the hybrid modeling approach JSB4-DL-fire (r_m=0.79) outperforming the currently used uncalibrated standard fire model in JSBACH4 (r_m=-0.07). We further quantify the importance of each predictor by applying layer-wise relevance propagation (LRP). Overall, land properties, such as fuel amount and water content in soil layers, stand out as the major factors determining burnt fraction in DL-fire, paralleled by meteorological conditions over tropical and high latitude regions. Our study demonstrates the potential of hybrid modeling in advancing fire prediction in ESMs by integrating deep learning approaches in physics-based dynamical models.

Plain Language Summary

We develop a fire-vegetation model based on a hybrid approach integrating artificial intelligence (AI) techniques into physics-based models. Given the weather conditions, vegetation states, and human factors, our model estimates daily burned area fraction. The spatiotemporal variations in burned area are closely reproduced, especially over fire-prone regions, such as Africa, South America, and Australia. Our model is able to represent regional variations in the drivers of fire occurrence, showing different importance of input predictors for different regions.

This approach shows the possibilities of using deep learning (DL) models to provide in-depth fire predictions in Earth system models.

1. Introduction

Fire is one of the main natural vegetation disturbance agents, and as such, a primary interactive component in the terrestrial ecosystem. Biomass burning affects the structure and dynamics of ecological processes (McLauchlan et al., 2020). Fire emissions alter atmospheric composition of trace gases and aerosol particles (Koppmann et al., 2005), with subsequent influences on land surface albedo (López-Saldaña et al., 2015), energy budgets (F. Li et al., 2017), climate (Liu et al., 2019; Voulgarakis & Field, 2015) and global biogeochemical cycles (Carcaillet et al., 2002; Crutzen & Andreae, 1990). Present-day global carbon emissions due to fire are approximately 1.5-3.0 PgC/yr (van der Werf et al., 2017). There is ample evidence that climate change has already resulted in increased fire risk and burned area in various areas around the world, and future increases are expected due to climate change (Seidl et al., 2017; Son et al., 2021). As fires are a significant source of greenhouse gases, there is the potential for positive (Harrison et al., 2018; Kurz et al., 1995) and negative feedbacks (Mahowald, 2011; Ward et al., 2012). Yet, important uncertainties remain to adequately represent fires in Earth system models (ESMs), with uncertainties in the representation of fire disturbance still dominating the overall uncertainties in the estimation of carbon fluxes from land (Hardouin et al., 2022).

Global fire models have been developed based on empirical and physical understanding of the fire process, and these have been incorporated within dynamic global vegetation models (DGVMs) (Hantson et al., 2016), In the early stage of global fire modeling, burnt area was estimated based on the amount of dry fuel and the length of fire season (Thonicke et al., 2001). The representation of frequency of fire occurrence was advanced by considering weather-driven fire risk (Lenihan, 1998). Venevsky et al. (2002) added characteristics of fire spread by adopting the Rothermel's rate-of-spread (RoS) equations (Rothermel, 1972). Based on the RoS, more advanced fire related physical representations were introduced (Pfeiffer et al., 2013; Thonicke et al., 2010) and implemented in various DGVMs (Drüke et al., 2019; Lasslop et al., 2014; Yue et al., 2016). Human activity impacts are also considered as nonlinear functions for fire ignition and

suppression based on population density, gross domestic product (GDP) and land-use changes (Kloster et al., 2010; le Page et al., 2015; F. Li et al., 2013).

Although there has been remarkable progress in global fire modeling, there are still many challenges remaining to represent the fire process and fire-vegetation interactions. For instance, fire characteristics, such as the completeness of combustion and plant mortality, are not robustly parameterized to reflect differences depending on vegetation types (Lasslop et al., 2014). Uncertainties in vegetation effects on fire remain as a main drawback in DGVMs (Forkel et al., 2019). Besides, while fire modeling has advanced with more sophisticated process based representations, there is still no agreement on the optimal level of complexity for a global fire model (Hantson et al., 2016).

Deep learning (DL), as a subset of machine learning (ML), has recently been incorporated in fire studies leading to significant advances within different aspects of fire science. For instance, spatial behavior of fire was successfully captured by using convolutional neural networks (Hodges & Lattimer, 2019; Radke et al., 2019). The long short-term memory modeling (LSTM) approaches also showed capability of predicting fire damage and duration (Z. Li et al., 2021; Liang et al., 2019). To address the spatiotemporal context for wildfire danger, (Kondylatos et al., 2022) applied a convolutional-LSTM network (Shi et al., 2015) integrating meteorological, environmental, and anthropogenic drivers. Other studies leveraged ML/DL methods to characterize various aspects of fire occurrence, such as fire weather (Son et al., 2022), lightning ignition (Coughlan et al., 2021), fire susceptibility (Zhang et al., 2021) and fuel availability (D'Este et al., 2021).

In this study, we develop a DL-based global fire model to improve biomass burnt damage simulation within a land surface model. Our model is composed of three independent modules to represent weather driven fire danger, land properties and anthropogenic effects on burnt area fraction estimation. Compared to a previous DL surrogate fire model (Zhu et al., 2022), our study has advances in two folds: 1) we incorporate LSTM based recurrent model architecture to consider time dependent memory effects from dynamic weather and vegetation processes; and 2) our model training was based on observational datasets, except for fuel load, allowing it to be coupled with any DGVM.

2. Methodology and Data

2.1. JSBACH4 and its simple fire scheme

JSBACH4 (Jena Scheme for Biosphere-Atmosphere Coupling in Hamburg version 4), which is the land surface model used in the ICON ESM, incorporates a simple fire model implemented to estimate fire damage based on combustible fuel availability and fuel dryness (Jungclaus et al., 2022). As one of the most simple fire representations, it can be applied in any global land surface model. The primary objective of the fire scheme is more focused on the disturbance effect on natural land cover changes, rather than fire occurrence and interactions, limiting its role on vegetation dynamics and carbon cycling in ecosystems. Instead, the previous version of JSBACH (JSBACH3.2) used the SPITFIRE fire model (Thonicke et al., 2010) to simulate global fire regimes, but it has not yet been implemented in JSBACH4.

In the simple fire scheme, the fuel availability is represented by the total litter density (L) and is compared to the litter threshold (L_0). The fuel dryness is estimated from surface level air relative humidity ($\overline{rh_t}$) smoothed with a persistence factor at each time step (Eq.1). When the humidity decreases lower than its threshold (rh_0), the fraction of burned area (FBA) is assumed to linearly increase as humidity decreases:

$$\overline{rh_t} = \overline{rh_{t-1}} \times p + \min(rh_t, 100) \times (1-p), \quad p = 0.95^{\frac{1}{48}} \tag{1}$$

$$FBA = FBA_{min} + \frac{1}{\tau} \times \frac{rh_0 - \overline{rh_t}}{rh_0} \quad if\ L > L_0\ and\ rh < rh_0 \quad otherwise\ 0 \tag{2}$$

where, τ denotes the frequency of fire occurrence: set as 6 years for woody and 2 years for grass type vegetation. We take the simple fire model (hereafter referred to as JSB4-simple) as the baseline for model evaluation. The standalone version of JSBACH4 is used to run JSB4-simple with the default configurations as used in JSBACH3.2 and described in Reick et al. (2021).

2.2. Deep learning (DL) fire model

The deep learning fire model (DL-fire) is composed of three modules: weather-driven fire danger, land properties and anthropogenic effects (Figure 1). The development of the modules for weather danger (W-LSTM) and land properties (L-LSTM) are based on the long short-term

memory network approach (LSTM) (Hochreiter & Schmidhuber, 1997). LSTM is an advanced recursive neural network to handle temporal dynamic behaviors from sequential data. The key aspect of the LSTM approach is its memory unit, called cell state that maintains information on states over timesteps, and its update is regulated by input and forget gates:

$$i_t = a_{sigmoid}(W_i \cdot [h_{t-1}, x_t] + b_i) \quad (3)$$

$$f_t = a_{sigmoid}\left(W_f \cdot [h_{t-1}, x_t] + b_f\right) \quad (4)$$

$$o_t = a_{sigmoid}(W_o \cdot [h_{t-1}, x_t] + b_o) \quad (5)$$

$$\tilde{c}_t = tanh(W_c \cdot [h_{t-1}, x_t] + b_c) \quad (6)$$

$$c_t = f_t \odot c_{t-1} + i_t \odot \tilde{c}_t \quad (7)$$

$$h_t = o_t \odot tanh(c_t) \quad (8)$$

where i, f, o denote the input gate, forget gate, output gate and c, h denote cell and hidden state. The terms W and b refer to the weight matrices and bias vectors for each gate and the cell states (e.g. W_i is the matrix of weights for the input gate), $a_{sigmoid}$ is the sigmoid function, $tanh$ is the hyperbolic tangent function, and $\odot$ denotes the element-wise product of vectors. The output dimension of the LSTM is set to 8 to be equal with the number of the plant functional types (PFTs), except for the bare land type.

The anthropogenic effect module uses two layers of fully connected feed-forward network:

$$h_t = act(W_1 \cdot x_t + b_1) \quad (9)$$

$$o_t = W_2 \cdot h_t + b_2 \quad (10)$$

where x denotes the input vector for anthropogenic variables and h is hidden layer vectors. The W and b terms are weight matrices and bias vectors for the input and hidden vectors. The function act represents a nonlinear transformation using a *softplus* function (Dugas

et al., 2000) in this study. The vector o is the output vector of the anthropogenic effect module that has the same dimension as the outputs of the W-LSTM and L-LSTM modules.

The final output, the fraction of burned area, is the computed sum of all PFTs, except for the bare land type, after multiplying results of the three modules and the fractions of PFTs (orange vector in Figure 1). Also, we use the fraction of bare land (f_bare) and snow (f_snow), fuel (above ground plant litter in JSBACH4) and relative humidity not only as LSTM input predictors, but also as constraints on fire occurrence and intensity:

$$FBA = (\sum o_w \times o_l \times o_a \times f\_PFTs) \times fire\ prone\ area \times dry\ fuel\ availability \quad (11)$$

$$fire\ prone\ area = 1 - f\_bare - f\_snow \quad (12)$$

$$dry\ fuel\ availability = fuel_{norm} \times S\left(1 - \frac{rh}{100}\right) \quad if\ rh > rh_0 \quad otherwise\ 0 \quad (13)$$

$$S(x) = \frac{1}{1+e^{-20\times(x-0.5)}} \quad (14)$$

where o_w, o_l, o_a denote output vectors of W-LSTM, L-LSTM and anthropogenic effect modules and f_PFTs denotes the fractions of PFTs. We use sigmoidal curve function (S) to transform relative humidity into a non-linear space. rh_0 is the threshold of relative humidity for fire occurrence set as 60 (%), $fuel_{norm}$ is normalized fuel using its maximum and minimum values during the training period (Eq.15).

2.3. Burnt fraction

For model training and evaluation, we used daily burned area from the Global Fire Emissions Database (GFED4) (Randerson et al., 2015) and calculated the burnt fraction for each grid cell. The GFED4 burned area product is based on the Moderate Resolution Imaging Spectroradiometer (MODIS) Collection 5.1 (MCD64A1 v5.1), globally available at 0.25°x0.25° spatial resolution.

Extreme data imbalance between instances of fire and no-fire is observed over all regions (Table 1). If the data with a large proportion of no-fire instances are directly used for model training, it is highly likely to mislead model outputs to converge into zero values. In order to reduce the risk of zero convergence, we adopt two strategies. We first used a gaussian kernel with 30 days of window size to smooth the burned area (step1 in Table 1). Subsequently, we

199 downsample no-fire instances according to ratios in Table 1 (step2 ratio), reducing the
200 imbalanced ratios to be close to 1:1 for all regions.
201
202 **2.4. Input variables**
203 The DL-fire uses 50 predictors which are divided into three sub-modules to predict burnt
204 fraction illustrated in detail in Table 2. The weather danger module (W-LSTM) uses 9 predictors,
205 including anomalies of temperature, specific and relative air humidity. Weather variables, such
206 as temperature, specific/relative air humidity, wind speed and precipitation, are obtained from
207 ERA5 (Hersbach et al., 2020) and lightning climatology is based on a dataset from the
208 spaceborne Optical Transient Detector (OTD) and Lightning Imaging Sensor (LIS) on the
209 Tropical Rainfall Measuring Mission (TRMM) satellite (Cecil et al., 2014). The anomalies are
210 calculated by extracting daily climatology (mean values on a day of year basis) during the years
211 1950-2020.
212 The land property module (L-LSTM) takes 23 predictors including the water volumes in
213 four soil layers are obtained from ERA5-Land (Muñoz-Sabater et al., 2021) and the Leaf Area
214 Index (LAI) is derived from the collection-5 MODIS LAI product (Myneni et al., 2015). We also
215 calculate daily anomalies for the water volumes and LAI using the above mentioned method
216 during 1950-2020 and 2003-2020, respectively. The topographic factors, such as elevation, slope
217 and roughness, are taken from (Amatulli et al., 2018). The amount of fuel is simulated by JSB4-
218 simple. The area distributions of plant functional types (PFTs) are obtained from Pongratz et al.
219 (2008), given as inputs for running JSBACH4 and we remap PFTs to be nine types as outlined in
220 Table 2.
221 The anthropogenic effect module (A-NN) takes into account a total of 18 predictors from
222 five different characteristics: population density (Klein Goldewijk et al., 2017), gross domestic
223 product (GDP) and human development index (HDI) (Kummu et al., 2018), total road density
224 (Meijer et al., 2018) and 14 fractions representing the state of land use (Hurtt et al., 2020).
225 All the input variables are regridded and aggregated to a daily timestep and 0.25 degree
226 spatial resolution to be consistent with the GFED4. Except for PFT fractions constrained in the
227 range of [0,1], we normalized predictors using maximum and minimum values of each region
228 based on the training period ($x_{r,train\_max}$ and $x_{r,train\_min}$, where r denotes a GFED region in
229 Figure S1), ideally to be in the range of [0,1]:

$$(x - x_{r,train_{min}})/(x_{r,train\_max} - x_{r,train\_min}) \qquad (15)$$

2.5. Model setup for training and simulation with JSBACH4

We develop 14 regional models based on GFED reference regions (Figure S1). To train the models, we use 12 years (2004-2015) of data considering data availability for burnt fraction and all the input predictors. We randomly select 80% of the dataset from the first 7 years (2004-10) for training and the remaining 20% are for validation during the model training stage. We apply a stratified random sampling approach is applied to preserve the same ratios between fire/no-fire incidents. The last 5 years (2011-15) are used for performance evaluation.

The dimension of the hidden layer is set to be 64 for all the three module architectures and dropout regularization is implemented for the anthropogenic module layers with 10% of probability to randomly inactivate neural network nodes. For the LSTM modules, the sequence length of training dataset is set to 14 days. We use the mean square error (MSE) loss function with ADAM optimizer (Kingma & Ba, 2014) by setting the learning rate to 0.001 and batch size to 1024. To avoid overfitting on the train dataset, we stop model training after a span of 30 epochs where no further improvement is observed in the validation dataset.

The DL-fire is trained without coupling to the dynamics of JSBACH4, as an offline learning approach. When the DL-fire is integrated into JSBACH4, all the land properties are provided by physics-based dynamics processes, except for topography. The other predictors are set to be forced by datasets used for model training and it allows the evaluation of simulation results from the year 2001. We perform experiments on the R2B4 ICON-grid system with spin-up time of 51 years, starting from the year 1950, and evaluate simulation results from 2001 to 2015. During the spin-up period (before the year 2001), we set all anthropogenic variables to be static at the state of January 1st 2001.

2.6. Evaluation metrics

To quantify the performance in simulating spatial variation, we apply the normalized mean error (NME) with area weights suggested by (Hantson et al., 2020):

$$NME = \sum_i A_i|o_i - m_i| \; / \; \sum_i A_i|o_i - \bar{o}| \qquad (15)$$

where o_i denotes the observed value, m_i the simulated value and A_i cell area at grid cell i. $\bar{o}$ is the mean of the observed values. A smaller value of NME describes better agreement with observation and zero is for perfect match between observation and model simulation. If NME is larger than 1, model performance is worse than simple prediction with statistical mean value.

We calculate the Pearson correlation coefficient between daily (r_d), monthly (r_m) and interannual (r_i) variability in predicted burnt fraction and GFED4, and the mean phase difference (MPD) to evaluate seasonal variation (Kelley et al., 2013). To quantify a distance between two phases, time unit is firstly transformed as an angle vector:

$$\theta_m = 2\pi(m-1)/12 \qquad (16)$$

where m denotes month (January-December). Then real (L_x) and imaginary (L_y) component vectors are calculated by:

$$L_x = \sum_m x_m \, cos(\theta_m) \qquad (17)$$

$$L_y = \sum_m x_m \, sin(\theta_m) \qquad (18)$$

The phase (P) is described by direction of the vectors (Eq.19) and MPD quantifies the phase difference by Eq.20:

$$P = arctan(L_x/L_y) \qquad (19)$$

$$MPD = \frac{1}{\pi}\sum_i A_i \times arcos[cos(\hat{P}_i - P_i)] \; / \; \sum_i A_i \qquad (20)$$

where $\hat{P}_i$ is phase from model simulation and P_i from observation at grid cell i.

2.7. Layer-wise relevance propagation

To interpret the decision making process of the DL-fire model, we apply the layer-wise relevance propagation (LRP) (Bach et al., 2015) to decompose contributions from the input

space. LRP computes relevance scores for each individual input by propagating relevance from the model output back through the neural network layers. While the total amount of relevance scores in each layer is kept consistent, the relevance in a layer is redistributed to the previous layer considering weights and input values, and this process repeats until getting the scores for the input layer. Here, we normalized relevance scores for each timestep so that the absolute values sum up to 1. Then we composite the normalized scores during the evaluation period to compare relative attribution with a global aspect.

3. Results

3.1. DL-fire model evaluation

Globally, the predicted burnt fraction shows a good overall accordance with the GFED4 estimates during the evaluation period (Figs 2a, b) with a NME of 0.64 (Table 3). The pattern of seasonal cycle is also accurately captured with 0.3 of MPD and 0.73 of r_d. Monthly aggregated predictions show a higher correlation score (r_m=0.80) than a previous DL model (0.76) (Joshi & Sukumar, 2021), although the evaluation period is different for both studies. However, high fractions, especially in the second half of the years 2011 and 2012, are underestimated (Fig 2c) indicating a degrading performance skill in interannual variability (r_i=0.35).

Regionally developed models vary in their performance skills. All the regional models show a NME lower than 1.0 and the best score is achieved in the northern part of South America (NHSA, 0.48), whereas NME is relatively high in regions where it shows large burnt fractions, such as Boreal North America (BONA), the southern part of South America (SHSA), the southern part of Africa (SHAF) and Central Asia (CEAS). The model for Central America (CEAM) shows high predictability in seasonal variation with 0.19 of MPD, and the BONA, SHSA, Africa and Equatorial Asia (EQAS) also perform well with a performance higher than 0.8 of r_d. The lowest daily correlations are obtained in the temperate North America (TENA, 0.47) and CEAS (0.41), showing underestimations in each of the fire seasons (Figs S2b, k). 8 out of 14 regional models perform well on predicting interannual fire patterns with higher than 0.8 of r_i. However, the least interannual predictability is shown across Southeast Asia (SEAS) and SHAF (r_i=-0.14, 0.08) due to lack in detecting high burnt fractions (Figs S2i, l). These results,

especially due to the SHAF, cause considerable drop in the interannual predictability at the global scale.

3.2. Coupling with JSBACH4

When the DL-fire model is coupled with JSBACH4 (JSB4-DL-fire), burnt fraction prediction skill is significantly enhanced in comparison to the simple fire model (JSB4-simple). JSB4-DL-fire improves NME score from 0.75 to 0.67 at the global scale, and NME decreases in 10 out of 14 regions (Table 4). Although burnt fractions in Africa and Siberia are underestimated, JSB4-DL-fire successfully captures the spatial variation of burnt fraction, especially across fire prone regions, such as Africa, South America, and Australia (Figs 3a, b).

Furthermore, burnt fractions in fuel-limited areas are improved to be close to zero in JSB4-DL-fire. JSB4-simple sets nonzero constant parameter for the minimum degree of fire damage (see Method), the results of JSB4-simple show higher than 0.1%/year of damage over almost all areas, including deserts and extremely cold regions (Fig S3a). Due to this oversimplified parameterization, arid areas and high latitudes, such as BONA, TENA, Europe (EURO), Middle East (MIDE) and Asia (BOAS and CEAS), show poor NME scores (2.34, 2.49, 2.06, 6.10, 1.40 and 1.39, respectively). These discrepancies are effectively addressed by JSB4-DL-fire with fuel and PFT constraints, improving NME to be lower than 1.0 across all the regions, except for MIDE.

The global spatial variation in fire seasonality is compared by visualizing the month with maximum fire damage per grid cell during the year 2001-15 (Figs 3c, d). JSB4-DL-fire shows overall coincide fire season distribution with GFED4, and the best score of MPD is achieved over CEAM (0.19, Table 4). Compared to JSB4-simple, the seasonal phase difference in AUST is also improved (MPD=0.26), but JSB4-DL-fire achieves slightly increased scores in 8 out of 14 regions. Nevertheless, the most notable improvement in JSB4-DL-fire is found in temporal correlations. While the global mean of the JSB4-simple simulation has a statistically insignificant relationship with GFED4 (r_d, $r_m \approx 0$ and r_i=0.17), the JSB4-DL-fire considerably increases the correlations (r_d=0.61, r_m=0.79, r_i=0.37). We also compare their seasonality during 2011-15 (DL evaluation period), showing that the month to month variability in JSB4-simple is

highly underestimated, showing a limited range in monthly burned area values, whereas spatial and seasonal patterns of JSB4-DL-fire generally match well with GFED4 (Fig S4).

Regionally, the performance of JSB4-DL-fire is most marked in SHSA and SHAF (Figs 4e, i) with scores higher than 0.8 of r_d (Table 4). JSB4-DL-fire also effectively reduces underestimation in NHAF and AUST (Figs 5h, n) as well as the overestimation in BONA, BOAS and CEAS (Figs. 5a, i, k). Among 14 regions, JSB4-DL-fire enhances r_d in 9 and r_m in 12 of them. In terms of interannual variability, the biggest improvement is found in BOAS, increasing r_i from 0.1 to 0.76, whereas the variability in SEAS and MIDE are the least predictable (-0.04 and -0.12, respectively). Although JSB4-DL-fire outperforms JSB4-simple in general, in comparison to the model validation results forced by observation (Table 3), the predictability of DL-fire is degraded over almost all the regions by integrating with JSBACH4. These changes in predictability by being coupled with JSBACH4 will be further discussed in terms of JSBACH4 internal biases in the next section.

3.3. Model interpretation

To understand how the DL fire model makes its predictions, we implement LRP for evaluating the contribution of each predictor. Globally, the fraction of bare land shows the highest absolute attribution with more than 16.3% of relevance score (Fig 5a). Its role, as a key component in identifying no or low risk of fire, is highlighted across regions, where there are large portions of arid lands or deserts, such as SHSA, MIDE, SHAF and AUST (Figs S5e, g, i, n). Fuel load also shows a high ratio of contribution (14.1%) based on its multiple roles as a constraint (7.4%) as well as an input of L-LSTM (6.7%). The volume of water in the 4th soil layer (SWL4) counts as the 3rd key factor associated with fire severity in that it can be considered an extreme condition when dryness has reached deeper soil level. Considering that the sum of soil dryness-related variable scores occupies 34.4% of the total relevance, the changes in soil dryness play as key drivers in the DL-fire.

Meteorological predictors, in spite of their small impacts in the global aspect (6.2%, Fig 5b), display significant importance in some tropical and high latitude regions. For instance, tropical rain forests are very fire-resistant during the wet season due to high humidity. Models trained over NHSA and EQAS show high relevance of relative humidity and temperature to

capture the climatic characteristics and their distinct seasonality (Figs S5d, m). The strong influence of meteorological predictors are also noticeable over BONA and BOAS, especially temperature contributes the most (12.3% and 16.4% respectively) (Figs S4a, j). These results are associated with fire-climate interactions in boreal forests where fire frequency and extent are affected depending on temperature variation (Hu et al., 2015; Kim et al., 2020) and their positive feedbacks under climate change (Oris et al., 2014).

4. Discussion & Conclusion

In this study, we introduce a deep learning based fire model (DL-fire) and implement it within the physics-based land surface model JSBACH4. The DL-fire predicts burnt fraction based on weather conditions, land properties and anthropogenic effects, performing well in predicting spatial and seasonal variation. When the DL-fire operates as a coupled module within JSBACH4 (JSB4-DL-fire), the quality of fire damage simulation improves noticeably compared to the simple fire scheme in JSBACH4. However, the predictability of JSB4-DL-fire is not as accurate as the validation results of DL-fire forced by observation. Since the only differences between the two are from land property predictors, either observed or simulated, its main reason is presumed to be internal biases of JSBACH4.

To investigate the impact of JSBACH4 internal biases on fire prediction, we compare the predictors from a validation dataset and the simulated by JSBACH4. In terms of global perspective, the JSB4-DL-fire predictions overall underestimate fire damages from May to September, and subsequently its rising and falling seasonal pattern is roughly a month lagged from September to February (Fig S6). These similar discrepancies are found in LAI over Africa. The simulated LAI in NHAF are overall underestimated with a month lagged peak in its seasonality (Fig S7h). In SHAF, LAI shows opposite seasonal behavior from July to November (Fig S7i), causing an underestimation of fire damage (Fig 4i).

Regionally, MIDE and SEAS show the most apparent discrepancies due to overestimation in JSB4-DL-fire. JSBACH4 shows a tendency to underestimate water contents in all the soil layers (Figs S8-11), except for the content of the first layer (SWL1) in MIDE (Fig S8g). Considering that water availability in the topmost layer plays a vital role on vegetation

(Seneviratne et al., 2010) and agricultural productivity (Battista et al., 2016), the biases of SWL1 can mislead DL-fire to exaggerate combustible fuel amount or its conditions on the ground. Similarly, overestimated durations of burnt fraction and LAI in SEAS coincide with each other (Figs 4l and S7l). To effectively address internal biases of physics-based models, it was suggested to merge deep learning as an external post-processing method (Reichstein et al., 2019; Son et al., 2022). However, this approach is not directly applicable in this study due to dynamical interactions between predictors and DGVMs. Instead, an online training approach, developing the deep learning model concurrently with running DGVMs will be our next step to advance the function of DL-fire in ESMs.

Representing interannual variability in global burnt area is yet a continuous effort for improvement in fire-enable DGVMs. None of the DGVMs has yet proven to successfully reproduce interannual variability (Hantson et al., 2020), and their limited skills cause uncertainties for the global carbon budget estimation (Bastos et al., 2020). Previous DL model showed ability to capture observed interannual patterns, but it is still early to assure its preeminence due to its short evaluation period (Joshi & Sukumar, 2021). Although JSB4-DL-fire either performs well at a global scale, significant regional improvements are observed with higher than 0.7 of r_i over 6 out of 14 regions (Table 4). These results suggest that ML/DL based hybrid approach can be a solution for the interannual variability problems in DGVMs.

Human influence fire regimes in various ways that either promote or limit fire. The population growth and urban expansion generally increase fire incidents (Bowman et al., 2011), whereas fire suppression and land-use changes decline fire activity (Andela et al., 2017). Our model underrates roles of these factors showing conspicuously low global relevance (0.05%, Fig 5b). These consequences can be due to a coarse time resolution of anthropogenic dataset. Since all the anthropogenic variables are interpolated from annual records or used as static values, they cannot provide any information associated to seasonal variation or anomalous daily events. Besides, some of the major man-made fire damages, particularly agricultural burnings, can be explained by weather seasonality and vegetation states (Korontzi et al., 2006). However, it should be pointed out that our model globally utilized C3 annual crops (c3ann) the most among anthropogenic drivers (Fig S12a) to identify crop related activities, and regionally in NHAF, BOAS, SEAS and EQAS (Fig S12i, k, m, n). Population follows as the second influential anthropogenic factor and HDI also show relatively higher relevances in developed regions

(0.02% in TENA and 0.07% in EURO), echoing their socioeconomic impacts on fire (F. Li et al., 2013; Teixeira et al., 2021). These results may suggest its potential of further improvement of human impacts on fire activities with more sophisticate dataset and adapted model architecture.

Regarding a global or local training approach, it can be argued which one in particular is a better option, either one single global model or multiple regional models. A global coverage model can be efficient in terms of model development and coupling with DGVMs, but for it not to lose regional characteristics, it may require more trainable parameters and higher complexity in architecture. We tested to train a global model with the same architecture as our local models, and its prediction accuracy significantly decreased (r_m=0.1). For the local approach, there are two major points to be considered: 1) the number of regions that should be considered and, 2) whether a unified or a specialized model design for each region should be developed. Exploration of these options would enable us to further upgrade prediction performances, however, this is not addressed in this study.

One of the main purposes of ESMs is to project climate changes based on future scenarios. However, in this study, we decide not to project future fire regime changes with DL-fire, although it is technically executable. This is because our model is currently composed of 14 regional models, and it cannot practically reflect global bioclimatic changes. Finally, we argue that further approaches should focus on developing and training one global DL model coupled with the host land surface model, and by that learning aspects of regional fire variability which would support conducting fully hybrid projection simulations.

Data Availability Statement

GFED4 dataset is available at https://www.globalfiredata.org/data.html. Also, ERA5 dataset is available at https://cds.climate.copernicus.eu/cdsapp#!/home, lightning climatology dataset (LIS-OTD) is available at https://ghrc.nsstc.nasa.gov/pub/lis/climatology/, LAI dataset from MODIS is available at https://ladsweb.modaps.eosdis.nasa.gov/archive/allData/6/MCD15A3H/, Topography dataset is available at https://doi.pangaea.de/10.1594/PANGAEA.867114, HYDE3.2 dataset is available at https://www.pbl.nl/en/image/links/hyde, GDP and HDI dataset is available at

https://datadryad.org/stash/dataset/doi:10.5061/dryad.dk1j0, GRIP4 dataset is available at https://www.globio.info/download-grip-dataset, LUH2 dataset is available at https://luh.umd.edu/. Also, the model simulation results are openly available in Zenodo at https://doi.org/10.5281/zenodo.7728155.

Acknowledgments

This work was supported by the European Union's H2020 research and innovation programme under grant agreement nos. 101003536 (ESM2025). We should secondly acknowledge SeasFire (Lazaro), DeepCube (Christian) and USMILE (Alex).

References

Amatulli, G., Domisch, S., Tuanmu, M.-N., Parmentier, B., Ranipeta, A., Malczyk, J., & Jetz, W. (2018). A suite of global, cross-scale topographic variables for environmental and biodiversity modeling. *Scientific Data*, *5*(1), 1–15.

Andela, N., Morton, D. C., Giglio, L., Chen, Y., van der Werf, G. R., Kasibhatla, P. S., DeFries, R. S., Collatz, G. J., Hantson, S., & Kloster, S. (2017). A human-driven decline in global burned area. *Science*, *356*(6345), 1356–1362.

Bach, S., Binder, A., Montavon, G., Klauschen, F., Müller, K.-R., & Samek, W. (2015). On pixel-wise explanations for non-linear classifier decisions by layer-wise relevance propagation. *PloS One*, *10*(7), e0130140.

Bastos, A., O'Sullivan, M., Ciais, P., Makowski, D., Sitch, S., Friedlingstein, P., Chevallier, F., Rödenbeck, C., Pongratz, J., & Luijkx, I. T. (2020). Sources of uncertainty in regional and global terrestrial CO2 exchange estimates. *Global Biogeochemical Cycles*, *34*(2), e2019GB006393.

Battista, P., Chiesi, M., Rapi, B., Romani, M., Cantini, C., Giovannelli, A., Cocozza, C., Tognetti, R., & Maselli, F. (2016). Integration of ground and multi-resolution satellite data for predicting the water balance of a Mediterranean two-layer agro-ecosystem. *Remote Sensing*, *8*(9), 731.

Bowman, D. M. J. S., Balch, J., Artaxo, P., Bond, W. J., Cochrane, M. A., D'antonio, C. M., DeFries, R., Johnston, F. H., Keeley, J. E., & Krawchuk, M. A. (2011). The human dimension of fire regimes on Earth. *Journal of Biogeography*, *38*(12), 2223–2236.

Carcaillet, C., Almquist, H., Asnong, H., Bradshaw, R. H. W., Carrion, J. S., Gaillard, M.-J., Gajewski, K., Haas, J. N., Haberle, S. G., & Hadorn, P. (2002). Holocene biomass burning and global dynamics of the carbon cycle. *Chemosphere*, *49*(8), 845–863.

Cecil, D. J., Buechler, D. E., & Blakeslee, R. J. (2014). Gridded lightning climatology from TRMM-LIS and OTD: Dataset description. *Atmospheric Research*, *135*, 404–414.

Coughlan, R., di Giuseppe, F., Vitolo, C., Barnard, C., Lopez, P., & Drusch, M. (2021). Using machine learning to predict fire-ignition occurrences from lightning forecasts. *Meteorological Applications*, *28*(1), e1973.

Crutzen, P. J., & Andreae, M. O. (1990). Biomass burning in the tropics: Impact on atmospheric chemistry and biogeochemical cycles. *Science*, *250*(4988), 1669–1678.

D'Este, M., Elia, M., Giannico, V., Spano, G., Lafortezza, R., & Sanesi, G. (2021). Machine learning techniques for fine dead fuel load estimation using multi-source remote sensing data. *Remote Sensing*, *13*(9), 1658.

Drüke, M., Forkel, M., von Bloh, W., Sakschewski, B., Cardoso, M., Bustamante, M., Kurths, J., & Thonicke, K. (2019). Improving the LPJmL4-SPITFIRE vegetation–fire model for South America using satellite data. *Geoscientific Model Development*, *12*(12), 5029–5054.

Dugas, C., Bengio, Y., Bélisle, F., Nadeau, C., & Garcia, R. (2000). Incorporating second-order functional knowledge for better option pricing. *Advances in Neural Information Processing Systems*, *13*.

Forkel, M., Andela, N., Harrison, S. P., Lasslop, G., van Marle, M., Chuvieco, E., Dorigo, W., Forrest, M., Hantson, S., & Heil, A. (2019). Emergent relationships with respect to burned area in global satellite observations and fire-enabled vegetation models. *Biogeosciences*, *16*(1), 57–76.

Hantson, S., Arneth, A., Harrison, S. P., Kelley, D. I., Prentice, I. C., Rabin, S. S., Archibald, S., Mouillot, F., Arnold, S. R., Artaxo, P., Bachelet, D., Ciais, P., Forrest, M., Friedlingstein, P., Hickler, T., Kaplan, J. O., Kloster, S., Knorr, W., Lasslop, G., … Yue, C. (2016). The status and challenge of global fire modelling. *Biogeosciences*, *13*(11), 3359–3375. https://doi.org/10.5194/bg-13-3359-2016

Hantson, S., Kelley, D. I., Arneth, A., Harrison, S. P., Archibald, S., Bachelet, D., Forrest, M., Hickler, T., Lasslop, G., & Li, F. (2020). Quantitative assessment of fire and vegetation properties in simulations with fire-enabled vegetation models from the Fire Model Intercomparison Project. *Geoscientific Model Development*, *13*(7), 3299–3318.

Hardouin, L., Delire, C., Decharme, B., Lawrence, D. M., Nabel, J. E. M. S., Brovkin, V., Collier, N., Fisher, R., Hoffman, F. M., & Koven, C. D. (2022). Uncertainty in land carbon budget simulated by terrestrial biosphere models: the role of atmospheric forcing. *Environmental Research Letters*, *17*(9), 094033.

Harrison, S. P., Bartlein, P. J., Brovkin, V., Houweling, S., Kloster, S., & Prentice, I. C. (2018). The biomass burning contribution to climate–carbon-cycle feedback. *Earth System Dynamics*, *9*(2), 663–677.

Hersbach, H., Bell, B., Berrisford, P., Hirahara, S., Horányi, A., Muñoz-Sabater, J., Nicolas, J., Peubey, C., Radu, R., & Schepers, D. (2020). The ERA5 global reanalysis. *Quarterly Journal of the Royal Meteorological Society*, *146*(730), 1999–2049.

Hochreiter, S., & Schmidhuber, J. (1997). Long short-term memory. *Neural Computation*, *9*(8), 1735–1780.

Hodges, J. L., & Lattimer, B. Y. (2019). Wildland fire spread modeling using convolutional neural networks. *Fire Technology*, *55*(6), 2115–2142.

Hu, F. S., Higuera, P. E., Duffy, P., Chipman, M. L., Rocha, A. v, Young, A. M., Kelly, R., & Dietze, M. C. (2015). Arctic tundra fires: natural variability and responses to climate change. *Frontiers in Ecology and the Environment*, *13*(7), 369–377.

Hurtt, G. C., Chini, L., Sahajpal, R., Frolking, S., Bodirsky, B. L., Calvin, K., Doelman, J. C., Fisk, J., Fujimori, S., & Klein Goldewijk, K. (2020). Harmonization of global land use change and management for the period 850–2100 (LUH2) for CMIP6. *Geoscientific Model Development*, *13*(11), 5425–5464.

Joshi, J., & Sukumar, R. (2021). Improving prediction and assessment of global fires using multilayer neural networks. *Scientific Reports*, *11*(1), 1–14.

Jungclaus, J. H., Lorenz, S. J., Schmidt, H., Brovkin, V., Brüggemann, N., Chegini, F., Crüger, T., De-Vrese, P., Gayler, V., & Giorgetta, M. A. (2022). The ICON earth system model version 1.0. *Journal of Advances in Modeling Earth Systems*, *14*(4), e2021MS002813.

Kelley, D. I., Prentice, I. C., Harrison, S. P., Wang, H., Simard, M., Fisher, J. B., & Willis, K. O. (2013). A comprehensive benchmarking system for evaluating global vegetation models. *Biogeosciences*, *10*(5), 3313–3340.

Kim, J.-S., Kug, J.-S., Jeong, S.-J., Park, H., & Schaepman-Strub, G. (2020). Extensive fires in southeastern Siberian permafrost linked to preceding Arctic Oscillation. *Science Advances*, *6*(2), eaax3308.

Kingma, D. P., & Ba, J. (2014). Adam: A method for stochastic optimization. *ArXiv Preprint ArXiv:1412.6980*.

Klein Goldewijk, K., Beusen, A., Doelman, J., & Stehfest, E. (2017). Anthropogenic land use estimates for the Holocene–HYDE 3.2. *Earth System Science Data*, *9*(2), 927–953.

Kloster, S., Mahowald, N. M., Randerson, J. T., Thornton, P. E., Hoffman, F. M., Levis, S., Lawrence, P. J., Feddema, J. J., Oleson, K. W., & Lawrence, D. M. (2010). Fire dynamics during the 20th century simulated by the Community Land Model. *Biogeosciences*, *7*(6), 1877–1902.

Koppmann, R., von Czapiewski, K., & Reid, J. S. (2005). A review of biomass burning emissions, part I: gaseous emissions of carbon monoxide, methane, volatile organic compounds, and nitrogen containing compounds. *Atmospheric Chemistry and Physics Discussions*, *5*(5), 10455–10516.

Korontzi, S., McCarty, J., Loboda, T., Kumar, S., & Justice, C. (2006). Global distribution of agricultural fires in croplands from 3 years of Moderate Resolution Imaging Spectroradiometer (MODIS) data. *Global Biogeochemical Cycles*, *20*(2).

Kummu, M., Taka, M., & Guillaume, J. H. A. (2018). Gridded global datasets for gross domestic product and Human Development Index over 1990–2015. *Scientific Data*, *5*(1), 1–15.

Kurz, W. A., Apps, M. J., Stocks, B. J., & Volney, W. J. A. (1995). Global climate change: disturbance regimes and biospheric feedbacks of temperate and boreal forests. *Biotic Feedbacks in the Global Climatic System: Will the Warming Feed the Warming*, 119–133.

Lasslop, G., Thonicke, K., & Kloster, S. (2014). SPITFIRE within the MPI E arth system model: M odel development and evaluation. *Journal of Advances in Modeling Earth Systems*, *6*(3), 740–755.

le Page, Y., Morton, D., Bond-Lamberty, B., Pereira, J. M. C., & Hurtt, G. (2015). HESFIRE: a global fire model to explore the role of anthropogenic and weather drivers. *Biogeosciences*, *12*(3), 887–903.

Lenihan, J. M. (1998). Simulating broad-scale fire severity in a dynamic global vegetation model. *Northwest Sci.*, *72*(2), 91–103.

Li, F., Lawrence, D. M., & Bond-Lamberty, B. (2017). Impact of fire on global land surface air temperature and energy budget for the 20th century due to changes within ecosystems. *Environmental Research Letters*, *12*(4), 44014.

Li, F., Levis, S., & Ward, D. S. (2013). Quantifying the role of fire in the Earth system–Part 1: Improved global fire modeling in the Community Earth System Model (CESM1). *Biogeosciences*, *10*(4), 2293–2314.

Li, Z., Huang, Y., Li, X., & Xu, L. (2021). Wildland fire burned areas prediction using long short-term memory neural network with attention mechanism. *Fire Technology*, *57*(6), 1–23.

Liang, H., Zhang, M., & Wang, H. (2019). A neural network model for wildfire scale prediction using meteorological factors. *IEEE Access*, *7*, 176746–176755.

Liu, Z., Ballantyne, A. P., & Cooper, L. A. (2019). Biophysical feedback of global forest fires on surface temperature. *Nature Communications*, *10*(1), 1–9.

López-Saldaña, G., Bistinas, I., & Pereira, J. M. C. (2015). Global analysis of radiative forcing from fire-induced shortwave albedo change. *Biogeosciences*, *12*(2), 557–565.

Mahowald, N. (2011). Aerosol indirect effect on biogeochemical cycles and climate. *Science*, *334*(6057), 794–796.

McLauchlan, K. K., Higuera, P. E., Miesel, J., Rogers, B. M., Schweitzer, J., Shuman, J. K., Tepley, A. J., Varner, J. M., Veblen, T. T., & Adalsteinsson, S. A. (2020). Fire as a fundamental ecological process: Research advances and frontiers. *Journal of Ecology*, *108*(5), 2047–2069.

Meijer, J. R., Huijbregts, M. A. J., Schotten, K. C. G. J., & Schipper, A. M. (2018). Global patterns of current and future road infrastructure. *Environmental Research Letters*, *13*(6), 064006.

Muñoz-Sabater, J., Dutra, E., Agustí-Panareda, A., Albergel, C., Arduini, G., Balsamo, G., Boussetta, S., Choulga, M., Harrigan, S., & Hersbach, H. (2021). ERA5-Land: A state-of-the-art global reanalysis dataset for land applications. *Earth System Science Data*, *13*(9), 4349–4383.

Myneni, R., Knyazikhin, Y., Park, T., & SIPS-NASA, B. U. and M. (2015). MOD15A3H MODIS/Combined Terra+ Aqua Leaf Area Index/FPAR Daily L4 Global 500m SIN Grid. In *NASA LP DAAC*.

Oris, F., Asselin, H., Ali, A. A., Finsinger, W., & Bergeron, Y. (2014). Effect of increased fire activity on global warming in the boreal forest. *Environmental Reviews*, *22*(3), 206–219.

Pfeiffer, M., Spessa, A., & Kaplan, J. O. (2013). A model for global biomass burning in preindustrial time: LPJ-LMfire (v1. 0). *Geoscientific Model Development*, *6*(3), 643–685.

Pongratz, J., Reick, C., Raddatz, T., & Claussen, M. (2008). A reconstruction of global agricultural areas and land cover for the last millennium. *Global Biogeochemical Cycles*, *22*(3).

Radke, D., Hessler, A., & Ellsworth, D. (2019). FireCast: Leveraging Deep Learning to Predict Wildfire Spread. *IJCAI*, 4575–4581.

Randerson, J. T., van der Werf, G. R., Giglio, L., Collatz, G. J., & Kasibhatla, P. S. (2015). Global fire emissions database, version 4.1 (GFEDv4). *ORNL DAAC*.

Reichstein, M., Camps-Valls, G., Stevens, B., Jung, M., Denzler, J., & Carvalhais, N. (2019). Deep learning and process understanding for data-driven Earth system science. *Nature*, *566*(7743), 195–204.

Reick, C. H., Gayler, V., Goll, D., Hagemann, S., Heidkamp, M., Nabel, J. E. M. S., Raddatz, T., Roeckner, E., Schnur, R., & Wilkenskjeld, S. (2021). *JSBACH 3-The land component of the MPI Earth System Model: documentation of version 3.2*.

Rothermel, R. C. (1972). *A mathematical model for predicting fire spread in wildland fuels* (Vol. 115). Intermountain Forest & Range Experiment Station, Forest Service, US ….

Seidl, R., Thom, D., Kautz, M., Martin-Benito, D., Peltoniemi, M., Vacchiano, G., Wild, J., Ascoli, D., Petr, M., & Honkaniemi, J. (2017). Forest disturbances under climate change. *Nature Climate Change*, *7*(6), 395–402.

Seneviratne, S. I., Corti, T., Davin, E. L., Hirschi, M., Jaeger, E. B., Lehner, I., Orlowsky, B., & Teuling, A. J. (2010). Investigating soil moisture–climate interactions in a changing climate: A review. *Earth-Science Reviews*, *99*(3–4), 125–161.

Shi, X., Chen, Z., Wang, H., Yeung, D.-Y., Wong, W.-K., & Woo, W. (2015). Convolutional LSTM network: A machine learning approach for precipitation nowcasting. *Advances in Neural Information Processing Systems*, *28*.

Son, R., Kim, H., Wang, S.-Y. S., Jeong, J.-H., Woo, S.-H., Jeong, J.-Y., Lee, B.-D., Kim, S. H., LaPlante, M., & Kwon, C.-G. (2021). Changes in fire weather climatology under 1.5° C and 2.0° C warming. *Environmental Research Letters*, *16*(3), 34058.

Son, R., Ma, P., Wang, H., Rasch, P. J., Wang, S., Kim, H., Jeong, J., Lim, K. S., & Yoon, J. (2022). Deep Learning provides substantial improvements to county-level fire weather forecasting over the western United States. *Journal of Advances in Modeling Earth Systems*, e2022MS002995.

Teixeira, J. C., Folberth, G. A., O'Connor, F. M., Unger, N., & Voulgarakis, A. (2021). Coupling interactive fire with atmospheric composition and climate in the UK Earth System Model. *Geoscientific Model Development*, *14*(10), 6515–6539.

Thonicke, K., Spessa, A., Prentice, I. C., Harrison, S. P., Dong, L., & Carmona-Moreno, C. (2010). The influence of vegetation, fire spread and fire behaviour on biomass burning and trace gas emissions: results from a process-based model. *Biogeosciences*, *7*(6), 1991–2011.

Thonicke, K., Venevsky, S., Sitch, S., & Cramer, W. (2001). The role of fire disturbance for global vegetation dynamics: coupling fire into a Dynamic Global Vegetation Model. *Global Ecology and Biogeography*, *10*(6), 661–677.

van der Werf, G. R., Randerson, J. T., Giglio, L., van Leeuwen, T. T., Chen, Y., Rogers, B. M., Mu, M., van Marle, M. J. E., Morton, D. C., & Collatz, G. J. (2017). Global fire emissions estimates during 1997–2016. *Earth System Science Data*, *9*(2), 697–720.

Venevsky, S., Thonicke, K., Sitch, S., & Cramer, W. (2002). Simulating fire regimes in human-dominated ecosystems: Iberian Peninsula case study. *Global Change Biology*, *8*(10), 984–998.

Voulgarakis, A., & Field, R. D. (2015). Fire influences on atmospheric composition, air quality and climate. *Current Pollution Reports*, *1*(2), 70–81.

Ward, D. S., Kloster, S., Mahowald, N. M., Rogers, B. M., Randerson, J. T., & Hess, P. G. (2012). The changing radiative forcing of fires: global model estimates for past, present and future. *Atmospheric Chemistry and Physics*, *12*(22), 10857–10886.

Yue, C., Ciais, P., Zhu, D., Wang, T., Peng, S. S., & Piao, S. L. (2016). How have past fire disturbances contributed to the current carbon balance of boreal ecosystems? *Biogeosciences*, *13*(3), 675–690.

Zhang, G., Wang, M., & Liu, K. (2021). Deep neural networks for global wildfire susceptibility modelling. *Ecological Indicators*, *127*, 107735.

Zhu, Q., Li, F., Riley, W. J., Xu, L., Zhao, L., Yuan, K., Wu, H., Gong, J., & Randerson, J. (2022). Building a machine learning surrogate model for wildfire activities within a global Earth system model. *Geoscientific Model Development*, *15*(5), 1899–1911.

Figures and Tables

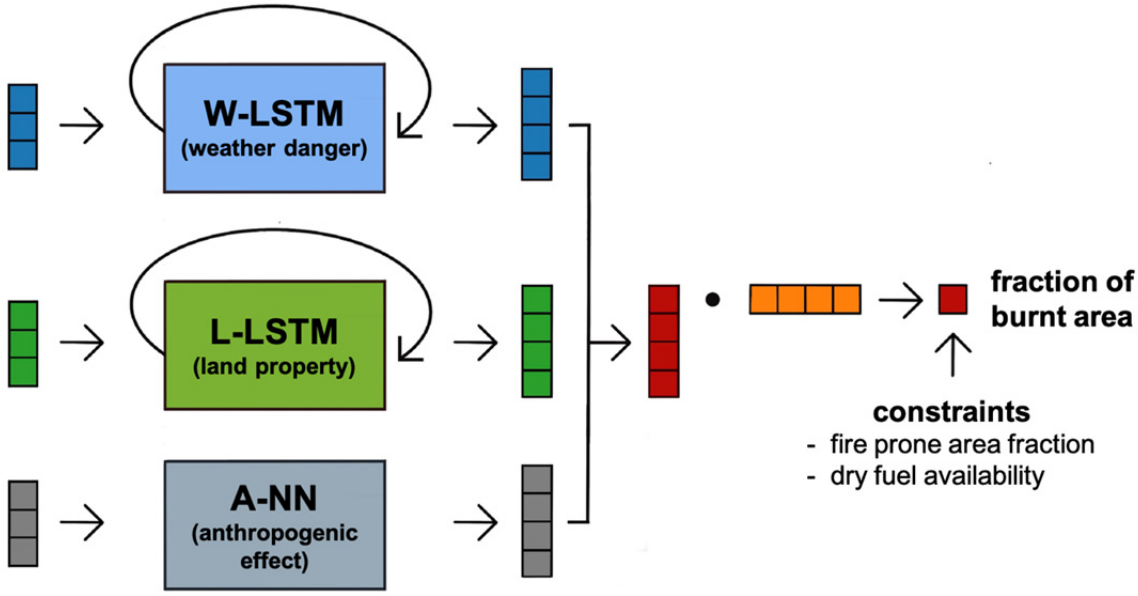

Figure 1. Flowchart of DL-fire model.

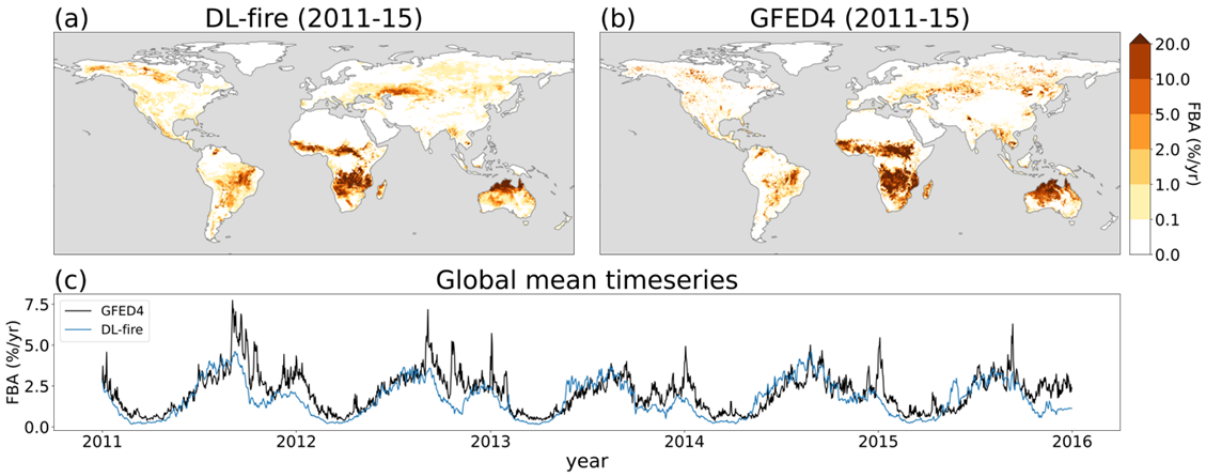

Figure 2. Spatial and temporal comparison between and GFED4 and DL-fire predictions. The maps of **a.** DL-fire and **b.** GFED4 visualize annual burnt fraction averaged over evaluation period (2011-15). **c.** compares global mean of burnt fraction from GFED4 (black) and DL-fire (blue).

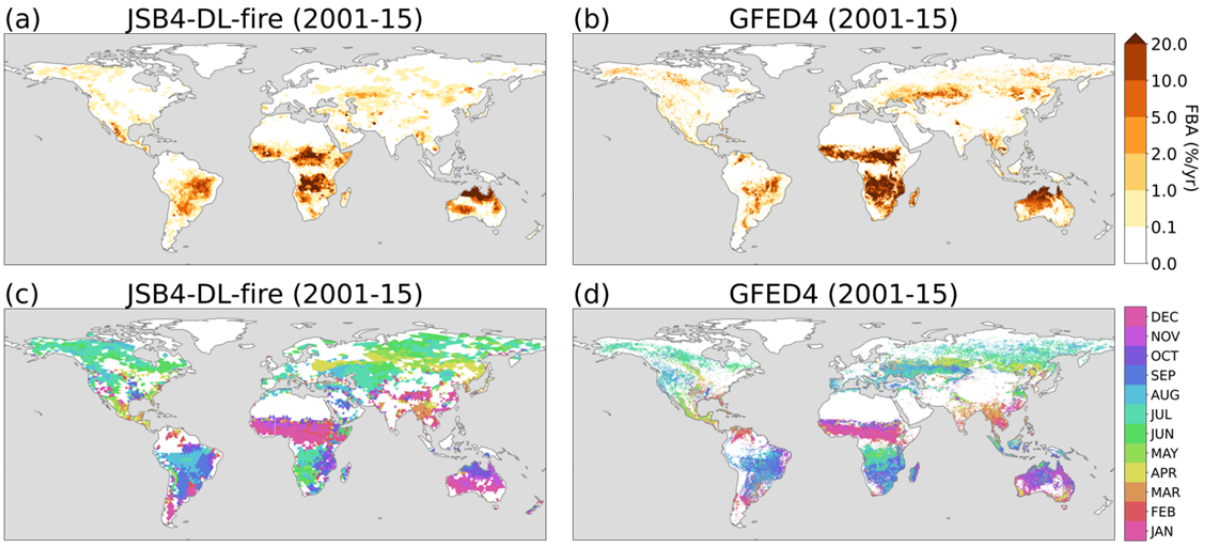

Figure 3. Spatial maps of burnt fraction and its seasonality. The maps on the top (**a.** JSB4-DL-fire and **b.** GFED4) show annual burnt fraction averaged over the years 2001-15, and the bottoms (**c.** JSB4-DL-fire and **d.** GFED4) visualize the peak month of burnt fraction. All areas with annual burnt fraction less than 0.1%/yr are masked out (white).

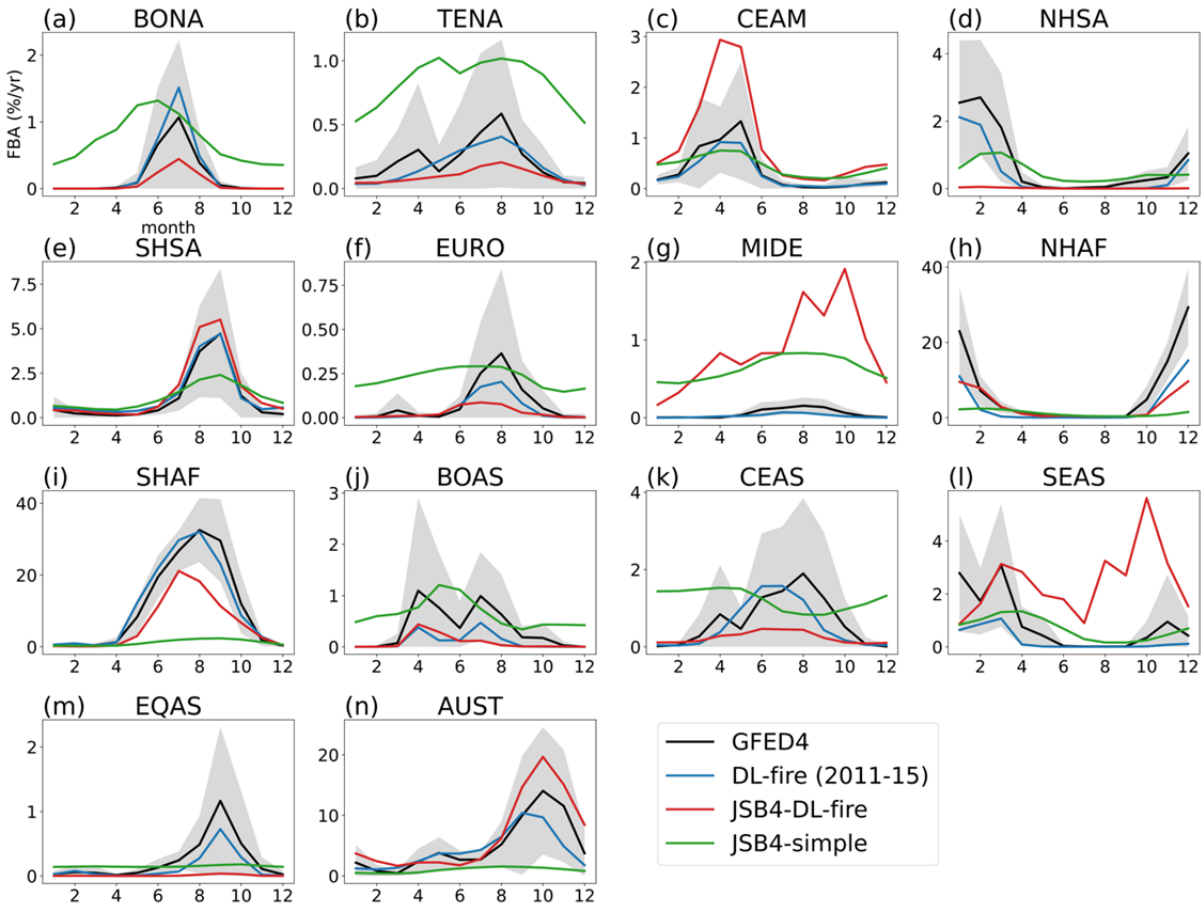

Figure 4. Comparison of monthly mean burnt fraction. Burnt fractions for GFED4 (black), JSB4-DL-fire (red), JSB4-simple (green) during 2001-15 and DL-fire (blue) during 2011-15 are averaged for each month and compared on each GFED regions (Figure S1). Gray shadings indicate 1-sigma intervals of the GFED4.

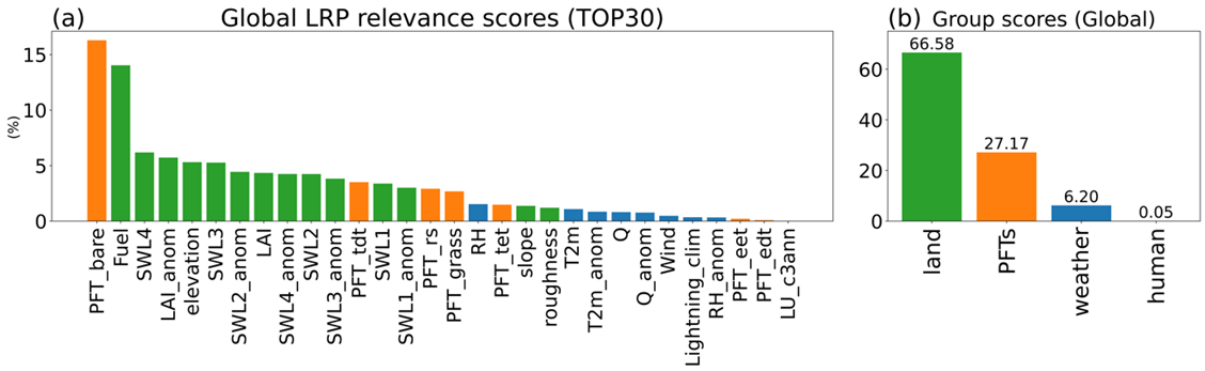

Figure 5. Global predictor importance assessment. a. shows predictors with the highest 30 LRP relevance scores and they are color-coded in four groups: weather conditions (blue), land properties (green), anthropogenic effects (gray) and PFTs (orange). Full names of PFTs and land use states (LU) are in Table 2 and Table S1. **b.** compares the relevance between the groups and their scores are displayed on top of bars.

828
829
830
831 **Table 1.** Ratio between grid-cell level fire/no-fire incidents per region. The last column is for
832 downsampling ratios used for step2.

	fire:no-fire	step1	step2	ratio (step2)
BONA	1:1313	1:301	1:1.0	300
TENA	1:412	1:61	1:1.23	50
CEAM	1:122	1:23	1:1.16	20
NHSA	1:85	1:20	1:1.02	20
SHSA	1:72	1:15	1:1.53	10
EURO	1:988	1:149	1:1.49	100
MIDE	1:1023	1:188	1:1.88	100
NHAF	1:27	1:8.4	1:1.69	5
SHAF	1:12	1:4.0	1:0.99	5
BOAS	1:721	1:128	1:1.27	100
CEAS	1:188	1:32	1:1.06	30
SEAS	1:104	1:24	1:1.19	20
EQAS	1:180	1:29	1:1.43	20
AUST	1:75	1:18	1:1.78	10

833
834
835
836
837
838
839
840
841
842
843
844
845
846
847
848
849
850
851
852

853
854
855
856
857 **Table 2.** Model input predictors.

Weather danger (W-LSTM)	temperature temperature anomaly	ERA5 (Hersbach et al., 2020)
	specific/relative humidity specific/relative humidity anomaly	
	wind speed	
	precipitation	
	lightning climatology	
Land property (L-LSTM)	volume of water in soil layers (4 levels) lv1: 0-7cm, lv2: 7-28cm, lv3: 28-100cm, lv4: 100-289cm volume of water anomaly (4 levels)	ERA5
	LAI LAI anomaly	MODIS (Myneni et al., 2015)
	elevation slope roughness	(Amatulli et al., 2018)
	fuel (above ground plant litter)	JSBACH4
	fraction of 9 plant functional types (PFTs) - snow (PFT_snow) - tropical evergreen trees (PFT_tet) - tropical deciduous trees (PFT_tdt) - extra-tropical evergreen trees (PFT_eet) - extra-tropical deciduous trees (PFT_edt) - raingreen shrubs (PFT_rs) - deciduous shrubs (PFT_ds) - grass (PFT_grass) - bare land (PFT_bare)	(Pongratz et al., 2008)
Anthropogenic effect (A-NN)	population density	HYDE3.2 (Klein Goldewijk et al., 2017)
	gross domestic product (GDP)	(Kummu et al., 2018)
	human development index (HDI)	

	total road density	GRIP4 (Meijer et al., 2018)
	land use (14) states (Table S1)	LUH2 (Hurtt et al., 2020)

858 **Table 3.** Evaluation metric scores for DL-fire.

	NME	MPD	r_d	r_m	r_i
Global	0.64	0.30	0.73	0.80	0.35
BONA	0.90	0.36	0.81	0.95	0.92
TENA	0.77	0.35	0.47	0.64	0.92
CEAM	0.72	0.19	0.82	0.90	0.86
NHSA	0.48	0.31	0.74	0.85	0.85
SHSA	0.83	0.23	0.85	0.89	0.52
EURO	0.76	0.33	0.60	0.76	0.92
MIDE	0.49	0.31	0.62	0.72	0.30
NHAF	0.58	0.31	0.88	0.93	0.38
SHAF	0.96	0.33	0.90	0.94	0.08
BOAS	0.69	0.31	0.63	0.77	0.82
CEAS	0.86	0.39	0.41	0.55	0.97
SEAS	0.56	0.22	0.60	0.82	-0.14
EQAS	0.55	0.28	0.90	0.97	0.99
AUST	0.50	0.29	0.66	0.76	0.50

859
860
861
862
863
864
865
866
867
868
869
870
871
872
873
874
875

876
877
878
879
880
881
882 **Table 4.** Evaluation metric scores for JSB4-DL-fire (JSB4-simple).

	NME	MPD	r_d	r_m	r_i
Global	0.67 (0.75)	0.31 (0.30)	0.61 (-0.07)	0.79 (-0.07)	0.37 (0.17)
BONA	0.72 (2.34)	0.36 (0.34)	0.62 (0.45)	0.85 (0.56)	0.71 (0.44)
TENA	0.71 (2.49)	0.35 (0.28)	0.37 (0.32)	0.64 (0.48)	0.82 (0.82)
CEAM	1.53 (1.08)	0.19 (0.24)	0.70 (0.61)	0.82 (0.72)	0.62 (0.37)
NHSA	0.61 (0.68)	0.21 (0.21)	0.55 (0.61)	0.72 (0.71)	0.51 (0.53)
SHSA	0.83 (0.85)	0.21 (0.20)	0.81 (0.71)	0.89 (0.77)	0.78 (0.62)
EURO	0.70 (2.06)	0.38 (0.36)	0.29 (0.32)	0.55 (0.50)	0.34 (0.32)
MIDE	7.96 (6.10)	0.32 (0.31)	0.12 (0.61)	0.34 (0.75)	-0.12 (-0.18)
NHAF	0.58 (0.67)	0.37 (0.44)	0.75 (0.35)	0.87 (0.39)	0.80 (0.65)
SHAF	0.76 (0.82)	0.33 (0.28)	0.84 (0.80)	0.91 (0.86)	0.35 (0.14)
BOAS	0.68 (1.40)	0.35 (0.36)	0.60 (0.27)	0.78 (0.35)	0.76 (0.10)
CEAS	0.61 (1.39)	0.39 (0.32)	0.57 (-0.24)	0.67 (-0.32)	0.29 (-0.22)
SEAS	2.05 (0.88)	0.25 (0.19)	-0.02 (0.40)	-0.03 (0.54)	-0.04 (0.32)
EQAS	0.50 (0.81)	0.25 (0.26)	0.41 (0.63)	0.77 (0.74)	0.80 (0.90)
AUST	0.81 (0.72)	0.26 (0.33)	0.70 (0.48)	0.78 (0.55)	0.42 (0.62)

883